Preparation and characterization of stable aqueous suspensions of up-converting Er^{3+}/Yb^{3+}-doped $LiNbO_3$ nanocrystals

M. Villegas · A.C. Caballero · M. Quintanilla · J.A. Sanz-García · E. Cantelar · F. Cussó

Abstract The preparation of $LiNbO_3:Er^{3+}/Yb^{3+}$ nanocrystals and their up-conversion properties have been studied. It is demonstrated that polyethyleneimine- (PEI) assisted dispersion procedures allow obtaining stable aqueous $LiNbO_3:Er^{3+}/Yb^{3+}$ powder suspensions, with average size particles well below the micron range (100–200 nm) and the isoelectric point of the suspension reaching values well above pH 7. After excitation of Yb^{3+} ions at a wavelength of 980 nm, the suspensions exhibit efficient, and stable, IR-to-visible (green and red) up-conversion properties, easily observed by the naked eye, very similar to those of the starting crystalline bulk material.

1 Introduction

Lithium niobate ($LiNbO_3$ = LNB) is a ferroelectric material that combines excellent electro-optic, acousto-optic and non-linear responses, which has motivated its use in a variety of applications, such as modulators or frequency-generators. Additionally, LNB crystals can be doped with luminescent ions (transition metal ions or rare-earths) enabling the development of further photonic applications, such as amplifiers and lasers [1–4].

Recently, considerable interest has been given to the fundamental investigation of these properties on the micro- and nano-scale, exploring the comparison with their bulk counterparts. Some groups have reported the possibility of synthesizing LNB nanoparticles by wet-chemical methods [5–8], but recently the possibility of achieving this goal by milling was also demonstrated [9], this method being cheaper and easier to transfer to industrial production than chemical synthesis. In this way, Fe- and Cu-doped nanoparticles with particle size in the range of 10–100 nm have been obtained, and they have been used to form stable suspensions in heptane, allowing the fabrication of new hybrid materials [9–11].

For biological applications, and particularly for imaging, one of the explored solutions relies on up-conversion processes using Yb^{3+} and Er^{3+} as doping ions [12–15]. In fact, this mechanism is well characterized in many materials, including LNB:Er^{3+}/Yb^{3+} bulk crystals [16–21]. Therefore, in the present work the fabrication of Er^{3+}/Yb^{3+}-doped LNB nanoparticles by milling and their subsequent optical characterization has been explored, with particular emphasis on whether the characteristic up-conversion phenomena remain unaltered by the process. Additionally, the possibility of preparation of stable water suspensions needed for most biological applications has been demonstrated.

2 Experimental

Nanoparticles have been prepared from a congruent $LiNbO_3$ monocrystal ([Li]/[Nb] = 0.945), doped with Er^{3+} and Yb^{3+}. The crystal was grown by the Czochralski method, as described elsewhere [22]. The concentrations of dopants were 0.14 mol% (Er^{3+}) and 0.7 mol% (Yb^{3+}), in the melt, which correspond to approximately 0.20 mol% (Er^{3+}) and 1,0 mol% (Yb^{3+}) in the crystal, according to their segregation coefficients [22].

M. Villegas · A.C. Caballero
Departamento de Electrocerámica, Instituto de Cerámica y Vidrio, CSIC, C/Kelsen, 5, 28049 Madrid, Spain

M. Quintanilla (✉) · J.A. Sanz-García · E. Cantelar · F. Cussó
Departamento de Física de Materiales, C-IV, Facultad de Ciencias, Universidad Autónoma de Madrid, Avda. Francisco Tomás y Valiente, 7, 28049 Madrid, Spain
e-mail: marta.quintanilla@uam.es

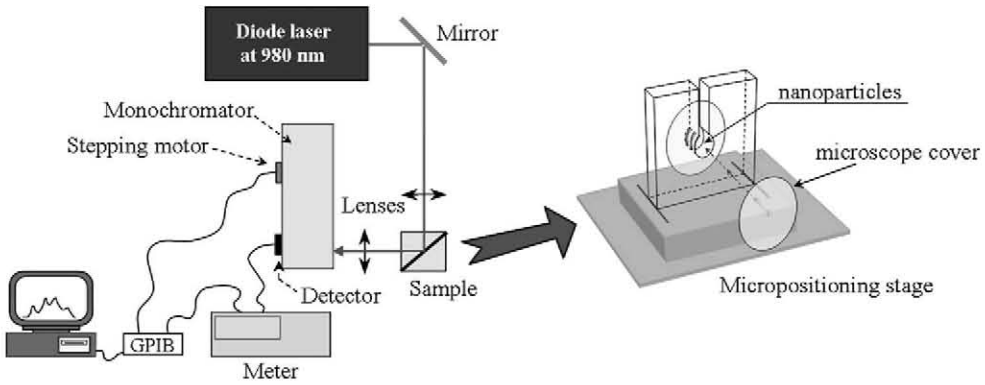

Fig. 1 Experimental set-up used for spectroscopic characterization of the up-converting nanocrystals. On the *right*, a detail of the sample holder is shown

Nanoparticles were obtained from this Er^{3+}/Yb^{3+}-doped $LiNbO_3$ raw monocrystal by applying several high-energy milling steps. A 20 mg fragment of the monocrystal specimen was initially grounded in a tungsten mortar, and the crushed powder was then milled for 2 hours on a planetary mill (Retsch), with ZrO_2 balls of 1.5–2.0 cm of diameter and water as milling media. Following this first milling stage, further particle decrease was achieved on a home-made attrition mill provided with a Teflon-coated vessel. Water and ZrO_2 balls of 1 mm diameter were used in these last experiments, applying milling times up to 12 hours.

The effectiveness of the milling process was followed by means of particle size measurements. After each milling step, the Er^{3+}/Yb^{3+}-doped $LiNbO_3$ dried powder (LNB: Er^{3+}/Yb^{3+}) was sieved through a 63 μm mesh, and the particle size distribution was determined by dynamic light scattering (DLS) [23] in a Mastersizer (Malvern). Prior to the size measurements, high power sonication was applied to disperse the agglomerates of particles (Ultrasonication Probe UP 400S). The morphology of the particles and the agglomeration state of the LNB:Er^{3+}/Yb^{3+} powders were also observed by scanning electron microscopy using a FE-SEM microscope (Hitachi S4700). The microscope was equipped with an Energy Dispersive Spectroscopy Microanalysis Probe (EDS).

Suspensions of the obtained nanocrystals were then prepared by suspending the 12 hours attrition-milled LNB: Er^{3+}/Yb^{3+} powders in water, with a powder concentration of 1 g/L. To prevent agglomeration and consequently to enhance the suspension stability, a polyethyleneimine (PEI) with a molecular weight of 2000 was added as a cationic dispersant [24, 25]. According to previous results reported in the literature [26], the optimum concentration of PEI was adjusted to around 1%, referred to the weight of powder. The dispersing conditions were evaluated in terms of the particle size distribution (DLS, Nanosizer ZS Malvern S) and the zeta potential versus pH. The zeta potential was determined following the Hückel approximation from the mobility data obtained by laser Doppler velocimetry on the Zetasizer. A 10^{-3} M KCl solution was used to run the zeta potential experiments, and the pH control was achieved by adding small amounts of 0.1 M HCl or KOH and by using a standard glass electrode pH meter. Up to three measurements were made for each sample.

Optical characterization was performed using the experimental set-up depicted in Fig. 1. Excitation was achieved using a Jenoptik diode laser at 980 nm to excite the Yb^{3+} ions. Luminescence was collected and focalized to the entrance slit of a SpectraPro 500-i monochromator and then detected with a photomultiplier tube linked to an AD converter. The digital outputs were averaged and stored on a PC. For lifetime measurements, after pulsed diode laser (LIMO) excitation the luminescence decay was detected by a fast response PM-tube (Hamamatsu H7422-50), and then recorded and averaged by a digital oscilloscope (Tektronix TDS-420).

Powdered samples have been pressed into a sampler holder constructed using a 1 mm-thick PMMA spacer with a 2 mm-diameter circular opening, enclosed by two microscope slide covers. Then the sample holder was placed in a fixed mount on the top of a micrometer stage, in order to optimize the luminescence signal. The diode laser beam was limited by a diaphragm assuring that the excitation area was smaller than the exposed sample area. The sample holder could be removed and replaced in this arrangement without altering the geometry of the experiment. It has been checked that luminescence spectra are reproducible, with integrated intensity variations smaller than 3%.

For liquid suspensions, the sample holder has been substituted by a standard spectroscopic quartz cell with 10 mm light path (Hellma).

All emission spectra have been corrected from the response of the monochromator grating and photomultiplier tube.

3 Results and discussion

3.1 Nanoparticles preparation and morphological characterization

Figure 2 shows the evolution of the particle size distribution for the LNB:Er^{3+}/Yb^{3+} powder after the subsequent steps

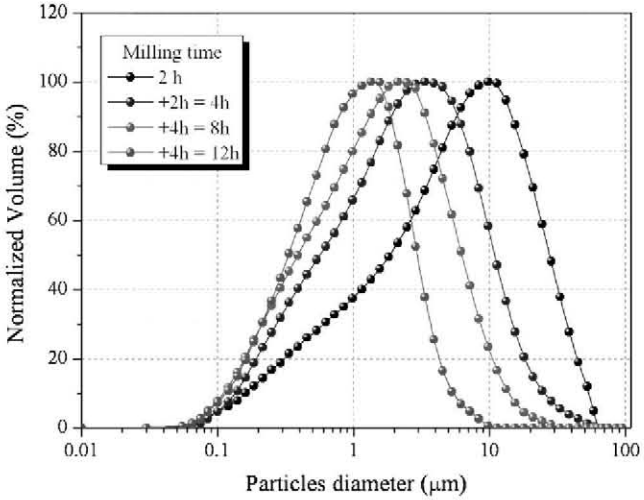

Fig. 2 Evolution of the particle size distribution with milling time

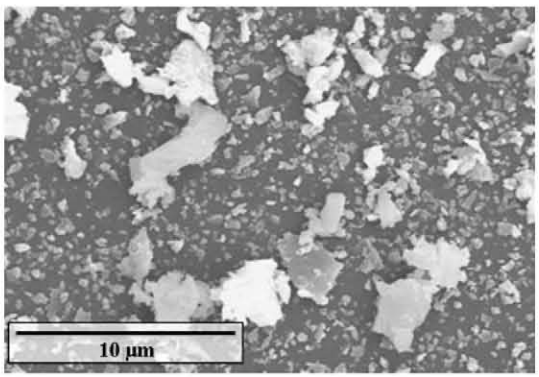

Fig. 3 FE-SEM micrograph of the 12 hours milled LNB:Er^{3+}/Yb^{3+} powder

in the attrition mill (the size distribution after the planetary mill step is omitted). As it can be seen, a wide distribution is obtained in all cases which may indicate the coexistence of different types of particles and/or agglomerates. Actually, it could be considered as an almost bimodal distribution, with a first group of big particles or agglomerates that decrease in size from 10 to 1.5 μm (d_{V50} mean values) as the milling proceeds, and a second family of much smaller particles that decrease in mean size from 0.5 to 0.1 μm (d_{V50} mean values) after the 12 hours of milling.

The situation was confirmed by the observation of the 12 hours milled LNB:Er^{3+}/Yb^{3+} powder in the electron microscope. The FE-SEM micrograph in Fig. 3 clearly shows the presence of big particles in the range of several microns which have not been efficiently milled. However, together with these big units, a large number of smaller particles with an average size below 1 μm can be as well observed. It should be noted that these small particles can also aggregate to form colonies of some microns in size.

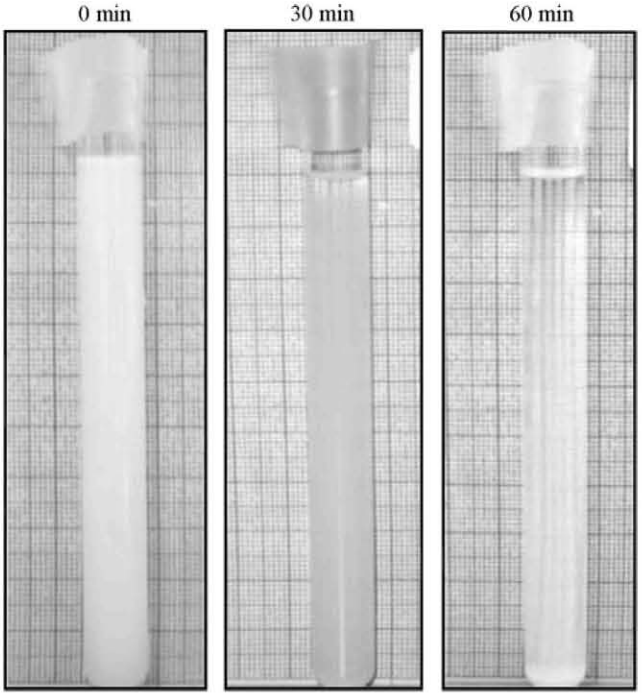

Fig. 4 Textures of the LNB:Er^{3+}/Yb^{3+} powder suspension with PEI from 0 min to 1 hour

Therefore, to obtain a narrow distribution of nanoparticles (a requisite to analyse whether the up-conversion phenomena remain unaltered after the milling process), those particles above the micron range should be removed. This has been achieved by preparing stable aqueous suspensions of the LNB:Er^{3+}/Yb^{3+} powders from which the big particles can be dislodged by a sedimentation process. As described in the experimental section, powder concentrations of 1 g/L of the 12 hours milled LNB:Er^{3+}/Yb^{3+} were used and 1 wt% PEI was added as dispersant to enhance the stability of the suspension. Once the suspension was prepared, the large particles were allowed to sediment by aging and thus they could be removed; at this point it must be noted that the time for the sedimentation of the large particles should be short enough to allow the smaller ones to remain in the suspension. In this sense, we performed several aging runs in a sealed glass at room temperature, and finally a sedimentation time of 1 hour was chosen (Fig. 4).

The suspension was then recovered by decantation, leaving the larger LNB:Er^{3+}/Yb^{3+} particles at the bottom of the glass beaker. Obviously, after the removal of the large particles, the powder concentration had changed and needed to be recalculated. In our case, the final concentration of the LNB:Er^{3+}/Yb^{3+} powder suspension was 0.6 g/L. The particle size distribution of this suspension was then measured by DLS and FE-SEM. As can be seen in Fig. 5, the large particles have been successfully removed and a narrow mono-modal size distribution centred at ~300 nm

was obtained. The absence of a bimodal curve also indicates that the formation of agglomerates was hindered due to the particle coating with the PEI polyelectrolyte. Moreover, the FE-SEM micrograph in Fig. 6 confirms that the LNB:Er^{3+}/Yb^{3+} powder was mainly composed of small aggregates of fine irregularly shaped particles in the range of 100 to 200 nm.

With regards to the stability of the dispersions, zeta potential measurements were conducted on the prepared aqueous suspension. The results are shown in the curves of Fig. 7. When no PEI is added, the isoelectric point of the LNB:Er^{3+}/Yb^{3+} powder is around 3.4, and the suspension shows a poor stability according to the zeta potential values ($\zeta < \pm 30$ mV). However, with the addition of PEI, the isoelectric point is shifted to pH as high as 10.5, and the zeta potential is greatly enhanced ($\zeta > 50$ mV below pH 9). This result is quite promising since it would allow for the use of these LNB:Er^{3+}/Yb^{3+} suspensions not only at the physiological pH but in a wider pH range.

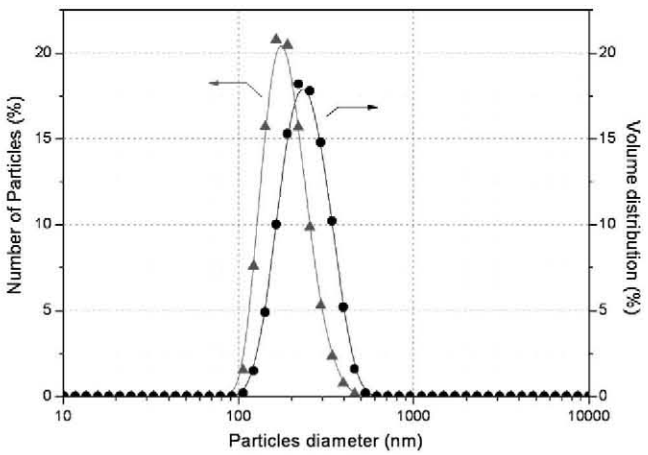

Fig. 5 Particle size distribution of the LNB:Er^{3+}/Yb^{3+} powder suspension after the removing of the large particles. Volume distribution (*right-hand axis*) peaks at around a particle size of 300 nm which, assuming approximately spherical particles, corresponds to a number of particles distribution centred at 200 nm (*left-hand side axis*)

3.2 Spectroscopic results

3.2.1 Dry nanoparticles

Figure 8 shows the luminescence emission spectra of LNB:Er^{3+}/Yb^{3+} nanoparticles after excitation at a wavelength of 980 nm. This pumping wavelength is mainly absorbed by the Yb^{3+} ions ($^2F_{7/2} \rightarrow {}^2F_{5/2}$ absorption band) giving rise to the efficient population of several Er^{3+} emitting levels via energy transfer (ET) and up-conversion (UC) mechanisms. A spectrum obtained from a bulk sample (a 1 mm thick slice obtained from the same boule and adjacent to the fragment used for the milling process) is also presented for comparison purposes.

According to the standard description of Er^{3+}/Yb^{3+} co-doped materials [16–19, 27, 28], after Yb^{3+} excitation, an efficient energy transfer to Er^{3+} takes place, via the $^2F_{5/2} \rightarrow {}^2F_{7/2}$ (Yb^{3+}):$^4I_{15/2} \rightarrow {}^4I_{11/2}$ (Er^{3+}) cross relaxation mechanism, as it is sketched in Fig. 9. The $^2F_{5/2}$ (Yb^{3+}) level is energetically resonant with the $^4I_{11/2}$ (Er^{3+})

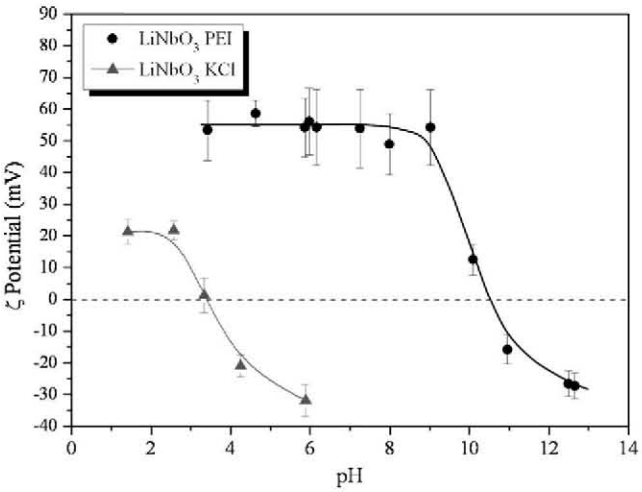

Fig. 7 ζ potential of LNB:Er^{3+}/Yb^{3+} powder suspension (*red line*) and LNB:Er^{3+}/Yb^{3+} powder suspension with PEI

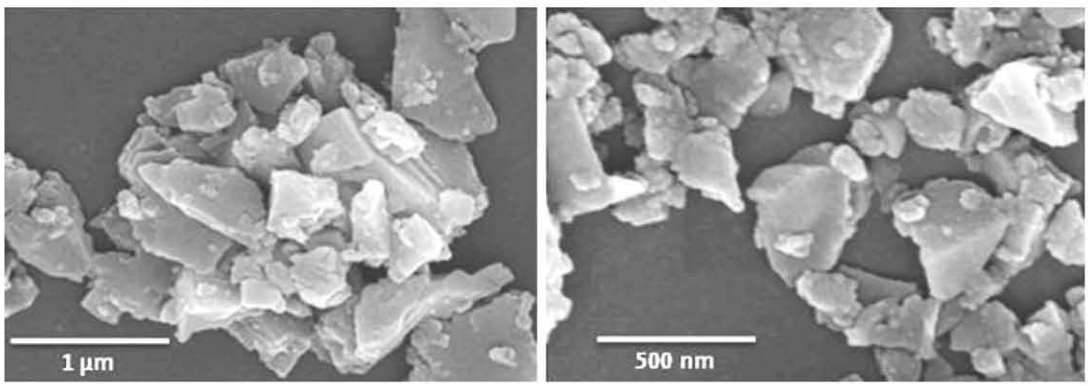

Fig. 6 FE-SEM micrograph of the LNB:Er^{3+}/Yb^{3+} powder from the aqueous suspension

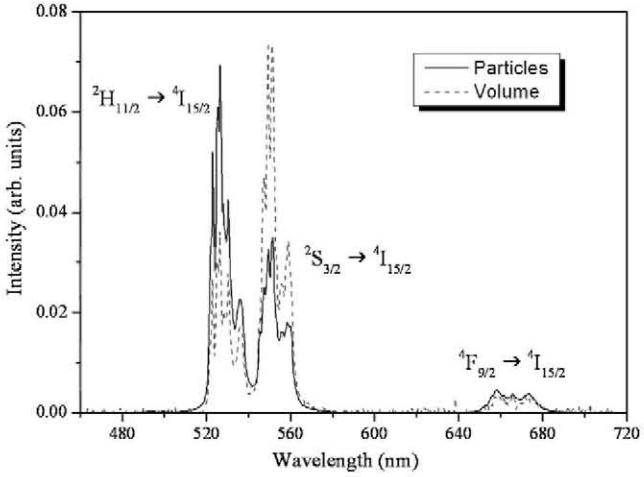

Fig. 8 Visible up-converted emission bands after excitation to the Yb^{3+} absorption band ($\lambda = 980$ nm). Two green emissions (500 nm < λ < 600 nm) and a red band (600 nm < λ < 700 nm), characteristic of Er^{3+} ions luminescence, are associated to the $^2H_{11/2}$, $^4S_{3/2} \rightarrow {}^4I_{15/2}$, and $^4F_{9/2} \rightarrow {}^4I_{15/2}$ transitions, respectively.

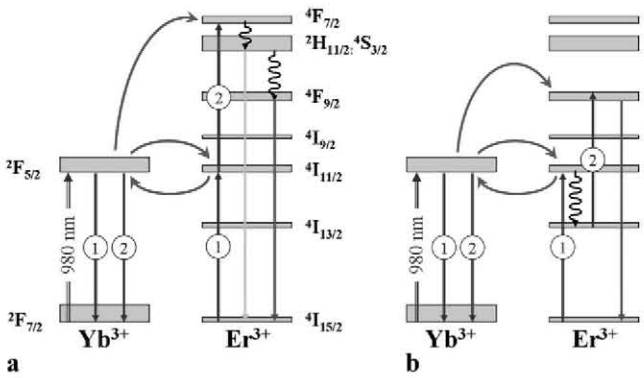

Fig. 9 Energy transfer up-conversion processes that populate the *green* (**a**) and *red* (**b**) Er^{3+} emitting levels after Yb^{3+} excitation

level, so that this energy transfer is highly efficient. Then, a second photon absorbed by an Yb^{3+} ion can be transferred to a previously excited Er^{3+} ion, which is promoted to the upper multiplets, generating the corresponding up-conversion emissions. This second energy transfer can take place via two different competitive mechanisms. Figure 9(a) illustrates how UC proceeds via a second transfer from Yb^{3+} ions, following the scheme: $^2F_{5/2} \rightarrow {}^2F_{7/2}$ (Yb^{3+}):$^4I_{11/2} \rightarrow {}^4F_{7/2}$ (Er^{3+}). This path populates the $^4F_{7/2}$ level of the Er^{3+} ion and, after an intermediate non-radiative relaxation, the $^2H_{11/2}$ and $^4S_{3/2}$ Er^{3+} levels, responsible of the two partially overlapped green emissions ($\lambda \approx 520$ and 540 nm).

Alternatively, the Er^{3+} green emitting levels can partially relax non-radiatively to the $^4F_{9/2}$ level from where the emission band in the red spectral region ($\lambda \approx 650$ nm) originates. Nevertheless, it has been previously demonstrated [27] that in LNB:Er^{3+}/Yb^{3+}, under 980 nm pump, the $^4F_{9/2}$

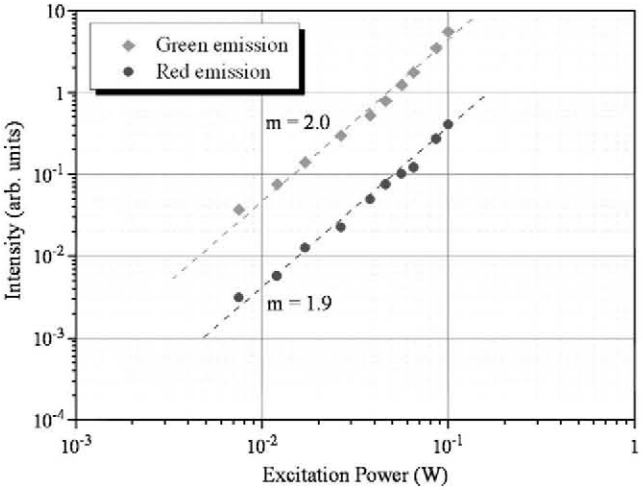

Fig. 10 Power dependence of the up-converted emissions in LNB:Er^{3+}/Yb^{3+} nanocrystals

level is mainly populated via an alternative UC path (see Fig. 9(b)): the $^4I_{11/2}$ level of Er^{3+} ions relaxes partially non-radiatively to the $^4I_{13/2}$ (Er^{3+}) multiplet, from where the energy transfer up-conversion process: $^2F_{5/2} \rightarrow {}^2F_{7/2}$ (Yb^{3+}):$^4I_{13/2} \rightarrow {}^4F_{9/2}$ (Er^{3+}) feeds the $^4F_{9/2}$ level originating the associated red emission.

The power dependence of the up-converted emissions in LNB:Er^{3+}/Yb^{3+} nanoparticles is presented in Fig. 10. As it can be observed, they follow the expected quadratic power dependence, associated to the above described two-photon excitation mechanism [28].

Comparing the spectra of the nanoparticles with that of the bulk sample, also included in Fig. 8, a change in the relative intensity of the 530 nm ($^2H_{11/2} \rightarrow {}^4I_{15/2}$) and 550 nm ($^4S_{3/2} \rightarrow {}^4I_{15/2}$) bands can be observed. These effects have been previously observed in a variety of host materials and attributed to a poor thermal contact between the nanoparticles, which favors a local temperature increase during optical excitation [29–31]. Since the energy gap between both emitting multiplets is relatively low (around 800 cm^{-1}), they are thermally coupled at ordinary temperatures following a Boltzmann distribution. Consequently, variations in temperature modify the population density of each green-emitting level and thus, the relative intensity of the bands. In order to confirm this assumption, the green up-converted emission bands have been measured at different excitation powers. The intensity ratio between the 530 nm ($^2H_{11/2} \rightarrow {}^4I_{15/2}$) and 550 nm ($^4S_{3/2} \rightarrow {}^4I_{15/2}$) bands is depicted in Fig. 11(a). As it can be observed, reducing the excitation power this ratio decreases, in accordance with the above given interpretation. Assuming that the temperature of the bulk sample, with superior heat dissipation conditions, is close to room temperature, it is possible to infer from the emission data presented in Fig. 8 that the nanoparticles ex-

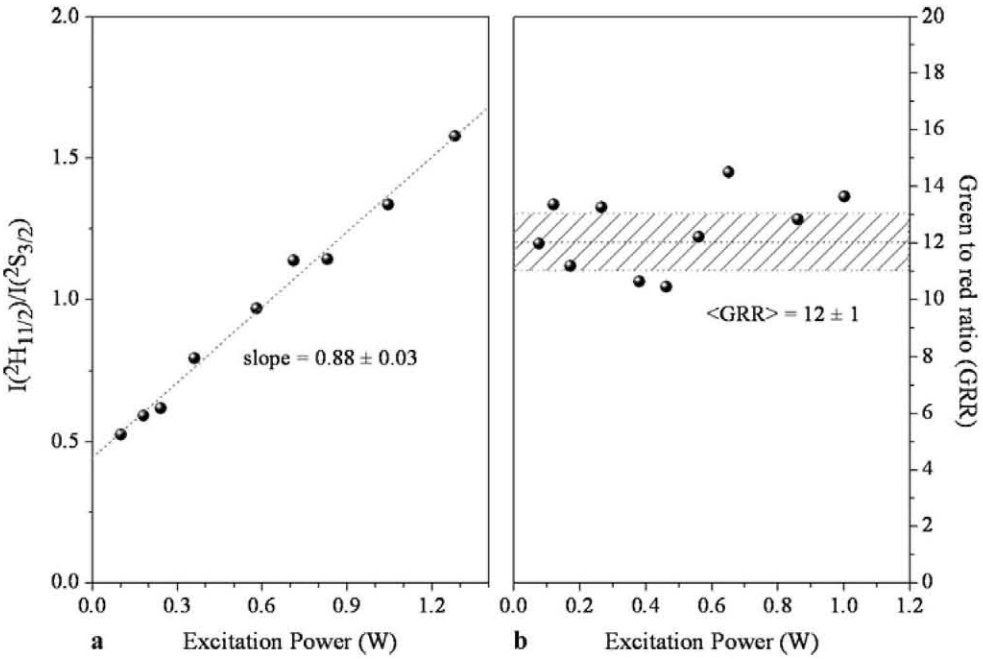

Fig. 11 Fluorescence intensity ratios between (**a**) green emission bands ($^2H_{11/2} \rightarrow {}^4I_{15/2}$ and $^4S_{3/2} \rightarrow {}^4I_{15/2}$); and (**b**) green (total) and red ($^4F_{9/2} \rightarrow {}^4I_{15/2}$) emissions ratio (GRR) as function of the IR pump power

perience a sizeable local temperature increase, which may be as high as 100 K for an excitation power of 100 mW.

Nevertheless, apart for the internal population re-distribution within the green emitting levels, the overall emission characteristics are not affected. In particular, it has been verified that the ratio between the integrated green and red emissions is approximately constant (Green to Red Ratio: GRR $\approx$ 12) within the range of powers used in the present work (up to 100 mW), as it is shown in Fig. 11(b).

3.2.2 Water suspensions

As it was previously indicated, in the section corresponding to material processing, it is possible to keep the nanoparticles in a stable water suspension. Nevertheless, the open question is whether the up-conversion processes above described for dry nanoparticles still remain when they are brought to suspension. The concern arises due to the fact that, as it is well known, the high-energy vibrational modes (3200–3600 cm^{-1}) associated to OH^- ions may induce strong multiphonon relaxations, particularly effective to quench the IR luminescence of Er^{3+} ions [32–34]. Therefore, the role of surface effects within the water-suspended particles could be important, as the surface to volume ratio increases when the particle size is reduced.

Figure 12 shows the luminescence of a water suspension of LNB:Er^{3+}/Yb^{3+} nanoparticles (with a particle concentration of 0.6 g/L) after excitation at a wavelength of 980 nm. As it is depicted in the inset, which corresponds to a photograph of the suspension, the up-converted emission is intense and it can be easily observed by the naked eye. The picture has been taken with a digital camera using the following parameters: ISO 400, aperture $f/4$ and exposure time 1 s.

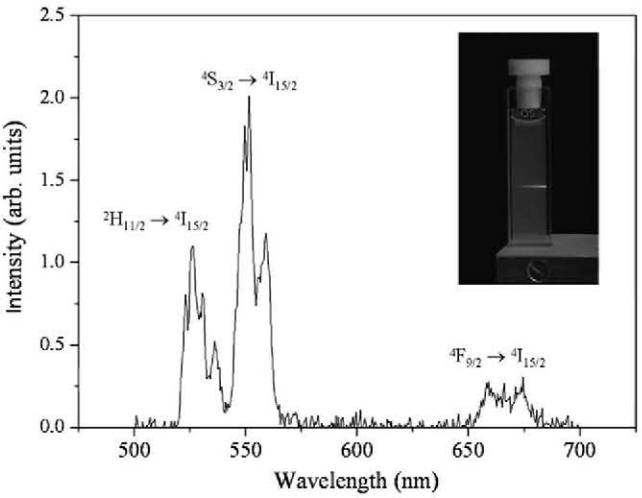

Fig. 12 Up-conversion emission spectrum of $LiNbO_3$:Er^{3+}/Yb^{3+} suspension in water (0.6 g/L + PEI) after excitation at 980 nm. The inset shows a photograph of the suspension illustrating the visible emission. This photograph has been taken with a digital camera using the following parameters: ISO 400, aperture $f/4$ and exposure time 1 s

The observed emission bands, as shown in Fig. 12, correspond to the characteristic green and red Er^{3+} emissions associated to the $^2H_{11/2}$:$^4S_{3/2} \rightarrow {}^4I_{15/2}$ and $^4F_{9/2} \rightarrow {}^4I_{15/2}$, respectively. It has been checked that their power dependences follow the same quadratic law observed in the dry-nanoparticles.

It can also be observed in the figure that the relative intensity of the green components resembles now that of bulk samples (see Fig. 8), indicating that thermal dissipation

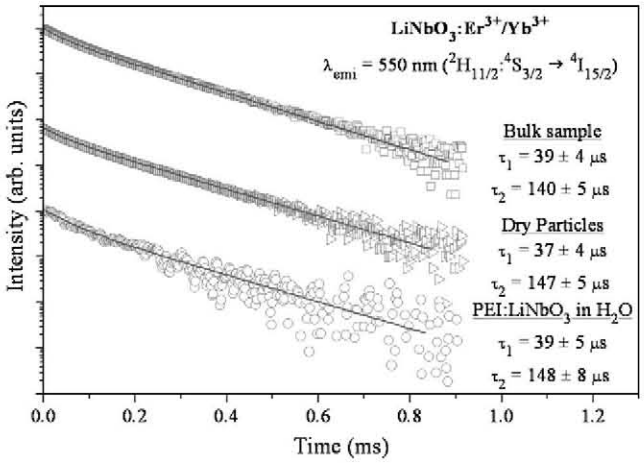

Fig. 13 Temporal decay of the green ($\lambda = 550$ nm, $^2H_{11/2}$:$^4S_{3/2} \rightarrow {}^4I_{15/2}$) Er^{3+} emission measured in bulk crystalline samples (*squares*), dry particles (*triangles*) and water-suspensions with PEI coated nanoparticles (*circles*). All decays are fitted with a bi-exponential decay (*red lines*) with a short ($\tau_1 \approx 38$ μs) and a long ($\tau_2 \approx 145$ μs) component

within the suspension is substantially more efficient than in powdered samples.

Taking this data into account, it seems that the shielding properties of PEI not only guarantee suspension stability, hindering aggregation, but also isolates sufficiently the rare-earth dopants from the solvent, allowing the sequential up-conversion steps needed to populate the green emitting $^2H_{11/2}$:$^4S_{3/2}$ multiplets despite the detrimental influence of OH^- radicals. As it has been mentioned above, OH^- vibrations are very efficient quenchers of the lower lying Er^{3+} excited states, which might therefore fully interrupt the up-conversion sequence (see Fig. 9). The observation of the green emission constitutes a first indication of the preservation of a sizeable population in the $^4I_{13/2}$ and $^4I_{11/2}$ Er^{3+} multiplets, needed for the energy transfer up-conversion processes that populate the green emitting levels.

In order to further explore the preservation of the optical characteristics in the nanoparticles, the luminescence dynamics of the up-converted emission under pulsed 980 nm excitation has been studied. Figure 13 shows the temporal decay of the green ($\lambda = 550$ nm) Er^{3+}-emission measured in bulk crystalline samples, dry particles and water-suspensions with PEI coated nanoparticles. As it can be observed, the obtained curves exhibit the same time dependence; which in all cases can be fitted with a bi-exponential decay. The shorter component agrees with the intrinsic lifetime of the emitting levels ($^2H_{11/2}$:$^4S_{3/2}$) [20], and corresponds to a first direct de-excitation stage. As it has been previously demonstrated [20, 21], after this initial period, a dynamical equilibrium between the population densities of donor levels (Er^{3+}:$^4I_{11/2}$ and Yb^{3+}:$^2F_{5/2}$, see Fig. 9) is established, and the subsequent decay of the green up-converted emission is governed by the statistically averaged lifetime of these levels. This corresponds to the longer component, lasting hundreds of microseconds. Its precise value is concentration dependent and may vary from 100 to 210 μs for Yb^{3+} concentration ranging from 0.1% to 2% Yb^{3+} mol% [20]. The measured value ($\tau_2 \approx 145$ μs) is in accordance with the doping concentration in the present samples.

The preservation of both decay components demonstrates that both the green emitting levels and the lower lying Er^{3+} and Yb^{3+} donor levels preserve their lifetimes, and therefore no appreciable quenching by OH^- vibrational modes occurs.

Finally, let us also indicate that luminescence signals from PEI-stabilized water suspended particles remain stable as long as the dispersion itself remains stable which, as indicated in the preceding sections, last for several days. For longer periods (several months), sedimentation finally takes place, but the particles can be turned back to suspension after few minutes of sonication, and the UC properties remain equally efficient, without being affected by this long period exposure to aqueous environment, which allows therefore for an easy storage.

4 Conclusions

According to the obtained results the milling and PEI-assisted dispersion procedures allow obtaining stable aqueous LNB:Er^{3+}/Yb^{3+} powder suspensions, in which the average size of the powder particles is well below the micron range (100–200 nm).

Furthermore, when PEI is used as dispersant, the isoelectric point of the suspension displaces at values well above pH 7, so it opens the possibility for the use of these up-converting LNB:Er^{3+}/Yb^{3+} aqueous suspensions in a physiological serum.

From the optical point of view, PEI-dispersed LNB:Er^{3+}/Yb^{3+} suspensions exhibit efficient IR-to-visible (green and red) up-conversion, after excitation of Yb^{3+} ions at a wavelength of 980 nm. The visible emissions, which can be easily observed by the naked eye, also remain stable and keep unaltered the properties of the crystalline material.

Acknowledgements This work has been funded by Comunidad de Madrid: S2009/TIC-1476 (MICROSERES-CM) and Ministerio de Ciencia e Innovación, MICINN, under projects MAT 2007-66845-CO2-01 and MAT2009-14102 (CRONOSOMATS). M. Quintanilla wants to thank the Spanish Ministerio de Educación for an FPU grant (AP2005-0763).

References

1. L. Thylen, Philos. Trans. R. Soc. Lond. A **329**, 83 (1989)
2. L. Arizmendi, Phys. Status Solidi A **201**, 253 (2004)

3. W. Sohler, H. Hu, R. Ricken, V. Quiring, C. Vannahme, H. Herrmann, D. Büchter, S. Reza, W. Grundkötter, S. Orlov, H. Suche, R. Nouroozi, Y. Min, Opt. Photonics News **19**, 24 (2008)
4. L. Tsonev, Opt. Mater. **30**, 892 (2008)
5. M. Niederberger, N. Pinna, J. Polleux, M. Antonietti, Angew. Chem. Int. Ed. **43**, 2270 (2004)
6. N. Pinna, M. Niederberger, Angew. Chem. Int. Ed. **47**, 5292 (2008)
7. B.D. Wood, V. Mocanu, B.D. Gates, Adv. Mater. **20**, 4552 (2008)
8. R. Grange, J.-W. Choi, C.-L. Hsieh, Y. Pu, A. Magrez, R. Smajda, L. Forró, D. Psaltis, Appl. Phys. Lett. **95**, 143105 (2009)
9. J.R. Schwesyg, H.A. Eggert, K. Buse, E. Sliwinska, S. Khalil, M. Kaiser, K. Meerholz, Appl. Phys. B **89**, 15 (2007)
10. S. Mansurova, K. Meerholz, E. Sliwinska, U. Hartwig, K. Buse, Phys. Rev. B **79**, 174208 (2009)
11. E. Sliwinska, S. Mansurova, U. Hartwig, K. Buse, K. Meerholz, Appl. Phys. B **95**, 519 (2009)
12. F. Wang, D.K. Chatterjee, Z.-Q. Li, Y. Zhang, X.-P. Fan, M.-Q. Wang, Nanotechnology **17**, 5786 (2006)
13. F. Wang, W.B. Tan, Y. Zhang, X.P. Fan, M.Q. Wang, Nanotechnology **17**, R1 (2006)
14. S.F. Lim, R. Riehn, C.K. Tung, W.S. Ryu, R. Zhuo, J. Dalland, R.H. Austin, Nanotechnology **20**, 405701 (2009)
15. F. Vetrone, J.A. Capobianco, Int. J. Nanotechnol. **5**, 1306 (2008)
16. L.F. Johnson, H.J. Guggenheim, T.C. Rich, F.W. Ostermayer, J. Appl. Phys. **43**, 1125 (1972)
17. F. Auzel, Proc. IEEE **61**, 758 (1974)
18. F. Auzel, J. Lumin. **45**, 341 (1990)
19. E. Cantelar, J.A. Muñoz, J.A. Sanz-Garcia, F. Cussó, J. Phys., Condens. Matter **10**, 8893 (1998)
20. E. Cantelar, F. Cussó, Appl. Phys. B **69**, 29 (1999)
21. E. Cantelar, F. Cussó, J. Phys., Condens. Matter **12**, 521 (2000)
22. E. Cantelar, J.A. Sanz-García, F. Cussó, J. Cryst. Growth **205**, 196 (1999)
23. A. Eshuis, G. Harbers, D.J. Doornink, P.F. Mijnlieff, Langmuir **1**, 289 (1985)
24. X. Wang, L. Zhou, Y. Ma, X. Li, H. Gu, Nano Res. **2**, 365 (2009)
25. X. Yu, M. Li, M. Xie, L. Chen, Y. Li, Q. Wang, Nano Res. **3**, 51 (2010)
26. M. Verde, A.C. Caballero, Y. Iglesias, M. Villegas, B. Ferrari, J. Electrochem. Soc. **157**, H55 (2010)
27. E. Cantelar, F. Cussó, J. Lumin. **102**, 525 (2003)
28. M. Pollnau, D.R. Gamelin, S.R. Luthi, H.U. Gudel, M.P. Hehlen, Phys. Rev. B **61**, 3337 (2000)
29. M.D. Shinn, W.A. Sibley, M.G. Drexhage, R.N. Brown, Phys. Rev. B **27**, 6635 (1983)
30. S.K. Singh, K. Kumar, S.B. Rai, Sens. Actuators A, Phys. **149**, 16 (2009)
31. N.O. Nuñez, H. Míguez, M. Quintanilla, E. Cantelar, F. Cussó, M. Ocaña, Eur. J. Inorg. Chem. 4517–4524 (2008)
32. V. Buissette, A. Huignard, T. Gacoin, J.P. Boilot, P. Aschehoug, B. Viana, Surf. Sci. **532–535**, 444 (2003)
33. H. Sun, L. Zhang, L. Wen, M. Liao, J. Zhang, L. Hu, S. Dai, Z. Jiang, Appl. Phys. B **80**, 881 (2005)
34. G. De, W. Quin, J. Zhang, J. Zhang, Y. Wang, C. Cao, Y. Cui, Solid State Commun. **137**, 483 (2006)